nature photonics

Supplementary information

https://doi.org/10.1038/s41566-024-01592-y

Observation of loss-enhanced magneto-optical effect

In the format provided by the authors and unedited

Contents:

S1. Experimental setup and measurement

Our experiment was conducted using a high-quality MO FP cavity shown in Fig. S1. The MO medium (TGG crystal) with a high transmittance, is placed in the center of the cavity and is18.5 mm long. An electric coil is wrapped around the TGG crystal and connected to a precision current source (ITECH, IT6302) to accurately provide the magnetic field $\vec{B}$ and the perturbation. The input laser beam is generated by a tunable external cavity diode laser (Model DLC pro, Toptica Company), focused into a 10-m long single mode fiber (SMF) for beam shaping and then collimated by a second fiber coupler. After subsequently passing through a quarter-wave plate (QWP), a half-wave plate (HWP), a polarization beam splitter (PBS) and another HWP, the laser beam is linearly polarized (LP) and orients at 45 degrees with the horizontal direction. The waist of the LP laser beam is adjusted by using two convex lenses to approximately 137 μm at the center of the cavity. The LP laser beam simultaneously excites the horizontal-polarized (HP) and vertical-polarized (VP) cavity modes with nearly equal intensity. The output spectra are detected by photoelectric detectors (PDs), recorded and analyzed by an oscilloscope.

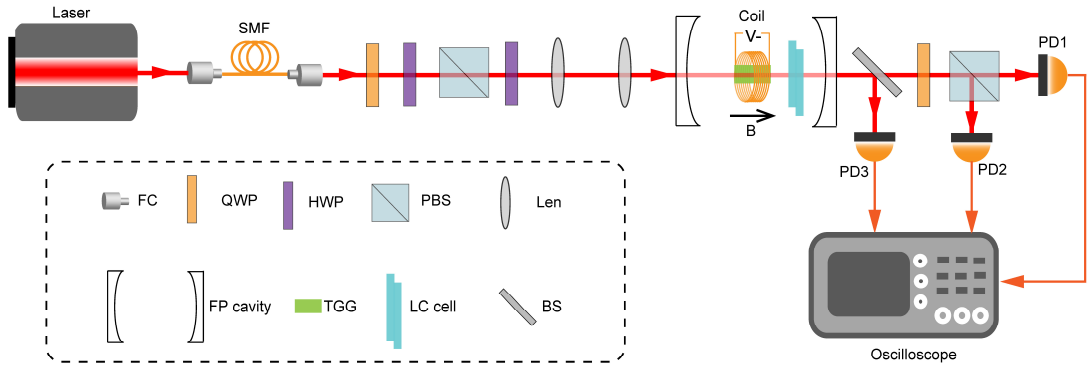

Fig. S1. Schematic of experimental setup. FC, fiber coupler; SMF, single mode fiber; QWP, quarter-wave plate; HWP, half-wave plate; PBS, polarization beam splitter; BS, beam splitter; PD, photoelectric detector; TGG, terbium gallium garnet.

In conventional Hermitian MO configuration with parity symmetry reserved, we observe the transmission spectra of LCP and RCP eigenmodes separately, using a quarter-wave plate and a polarization beam splitter. The separated signals are individually detected by PD1 and PD2. The spectrum of the total transmitted field is detected by PD3 for comparison. We precisely retrieve the resonance frequency of the eigenmodes by fitting the output spectra with single Lorentzian profiles in the conventional MO configuration. In the loss-enhanced MO configuration, the two eigenmodes are non-orthogonal. We detect the total transmission spectra using PD3 and fit them with superposition of two Lorentzian profiles to determine their resonant frequencies. This method has been widely used to determine the figure-of-merits of a light spectrum [1]. During the fitting process, the sum of linewidths of the two Lorentzian profiles is constrained by $\kappa_{\mathrm{H}}+\kappa_{\mathrm{V}}$. All the measurements are conducted in open environment without magnetic shielding.

S2. Magnetically induced polarization rotation and ellipticity

In the main text, we neglect the magnetically induced absorption and consider g a real number. Next, we present a quantitative analysis.

In the setup shown in Fig. S1, the optical FP cavity supports the HP and VP modes. The MO is inserted in the FP cavity. As introduced by Zvezdin and Kotov [2], the MO effect modifies the electric constitutive relation from $\vec{D}=\varepsilon_0\varepsilon\vec{E}$ to $\vec{D}=\varepsilon_0\varepsilon\vec{E}+i\varepsilon_0\varepsilon_s Q\vec{E}\times\vec{B}/B$, connecting the electric field $\vec{E}$ and the displacement $\vec{D}$ via the MO constant Q. The MO constant can be complex, $Q=Q_{\mathrm{R}}+iQ_{\mathrm{I}}$. Q_{I} and Q_{R} are characterized by the magnetically induced polarization rotation and ellipticity of the

transmitted field of a linearly-polarized light through the MO medium. The Faraday rotation and ellipticity can be evaluated as the complex angle $\theta = \theta_{\mathrm{R}} + i\theta_{\mathrm{I}}$ such that $Q_{\mathrm{I}}/Q_{\mathrm{R}} = \theta_{\mathrm{I}}/\theta_{\mathrm{R}}$. According to our theory in Method, the MO medium causes the coupling between these two cavity modes under a magnetic field with amplitude B. The coupling strength is gB. The coefficient g is related to the complex MO constant Q. Generally, it is also complex and can be denoted as $g_{\mathrm{R}} + ig_{\mathrm{I}}$. Thus, we have $g_I/g_R = \theta_I/\theta_R$.

To identify the real and imaginary parts of the coupling coefficient, we experimentally use a polarimeter to measure azimuth and ellipticity of the transmitted light through the MO medium under various magnetic fields. The incident light is vertically polarized. We have measured the azimuth and ellipticity of light after passing through an 18.5 mm long TGG crystal (Fig. S2a). The Faraday rotation and ellipticity under various magnetic field are shown in Fig. S2b. The Faraday rotation is proportional to the magnetic B at a slope of $0.083^{\circ}/\mathrm{T}$, in coincidence with the measured Verdet constant of $C_{\mathrm{V}} = 78.82$ rad/Tm. The ellipticity is too small to be detected when $B < 10$ mT. The ratio $g_I/g_R = \theta_I/\theta_R$ is 3.0×10^{-3} when $B = 23.5$ mT and 6.7×10^{-3} when $B = 31.3$ mT. In our experiments, we are interested in the region $B < 8$ mT. Thus, we can neglect the imaginary part g_{I} and consider g as a real number.

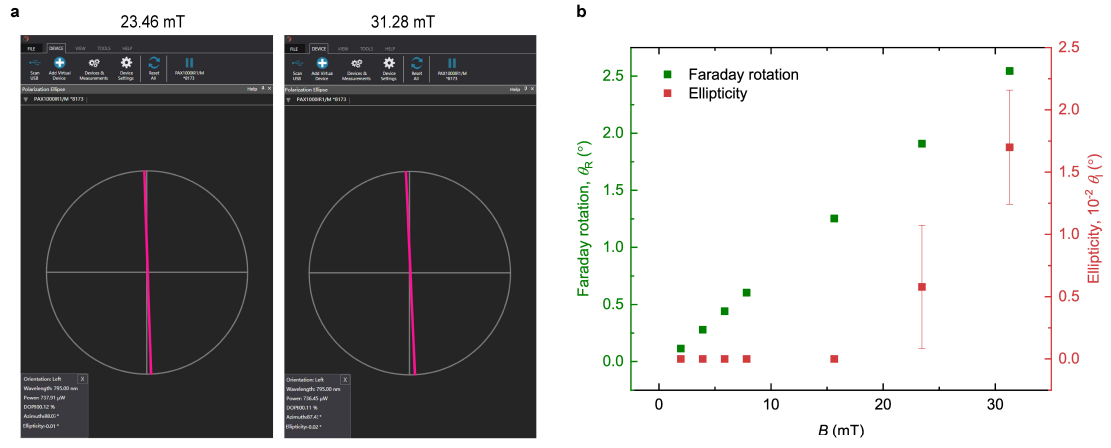

Fig. S2. Faraday rotation and ellipticity of the transmitted field of a vertically polarized input light after passing through an 18.5 mm long TGG crystal under various magnetic field B. **a**, The result of a single measurement by a polarimeter. **b**, Data points are presented as the mean ± standard deviation obtained from 20 independent repeated measurements.

S3. Transmission spectral analysis and eigenfrequency retrieval

S3.1 Transmission spectral analysis

In this section, we commence by presenting a theoretical model elucidating the output power spectrum for the loss-enhanced MO configuration. The system comprises of an FP cavity embedded with an MO medium, as shown in Fig. 1 in the main text. The FP cavity supports two orthogonal cavity modes, namely the HP and VP modes, with frequencies ν_{H} and ν_{V}. The input and output coupling rates for both modes are assumed to be equal, all denoted as κ_e. The internal losses are represented as $\kappa_{i,\mathrm{H}}$ for the HP mode and $\kappa_{i,\mathrm{V}}$ for the VP mode. Therefore, the total loss rates of the HP and VP modes can be expressed as $\kappa_{\mathrm{H}} = 2\kappa_e + \kappa_{i,\mathrm{H}}$ and $\kappa_{\mathrm{V}} = 2\kappa_e + \kappa_{i,\mathrm{V}}$, respectively. The Hamiltonian of the system of two coupled cavity modes, without the input and the noise taken into account, can be represented by a 2×2 matrix:

$$H_s = h\begin{bmatrix} \nu_{\mathrm{H}} - i\kappa_{\mathrm{H}} & igB \\ -igB & \nu_{\mathrm{V}} - i\kappa_{\mathrm{V}} \end{bmatrix}. \tag{S1}$$

The eigenfrequencies can be calculated as

$$\nu_{\pm} = \nu_0 - i\kappa \pm \sqrt{g^2B^2 + \left(\Delta\nu_0 + i\Delta\kappa\right)^2}, \tag{S2}$$

where $\nu_0 = \left(\nu_{\mathrm{H}} + \nu_{\mathrm{V}}\right)/2$, $\Delta\nu_0 = \left(\nu_{\mathrm{H}} - \nu_{\mathrm{V}}\right)/2$, $\kappa = \left(\kappa_{\mathrm{H}} + \kappa_{\mathrm{V}}\right)/2$, and $\Delta\kappa = \left(\kappa_{\mathrm{V}} - \kappa_{\mathrm{H}}\right)/2$. We use a_{H} and a_{V} to denote the amplitudes of the HP and VP modes, respectively. The equation of motion, with inputs α and β exciting the HP and VP modes respectively, is given by:

$$\frac{d}{dt}\begin{bmatrix} a_{\mathrm{H}} \\ a_{\mathrm{V}} \end{bmatrix} = -i\begin{bmatrix} \nu_{\mathrm{H}} - i\kappa_{\mathrm{H}} & igB \\ -igB & \nu_{\mathrm{V}} - i\kappa_{\mathrm{V}} \end{bmatrix}\begin{bmatrix} a_{\mathrm{H}} \\ a_{\mathrm{V}} \end{bmatrix} + \sqrt{2\kappa_e}\begin{bmatrix} \alpha \\ \beta \end{bmatrix}. \tag{S3}$$

Equation (S3) can be rewritten in the frequency domain as

$$-i\begin{bmatrix} \nu - \nu_{\mathrm{H}} + i\kappa_{\mathrm{H}} & -igB \\ igB & \nu - \nu_{\mathrm{V}} + i\kappa_{\mathrm{V}} \end{bmatrix}\begin{bmatrix} a_{\mathrm{H}}(\nu) \\ a_{\mathrm{V}}(\nu) \end{bmatrix} = \sqrt{2\kappa_e}\begin{bmatrix} \alpha \\ \beta \end{bmatrix}. \tag{S4}$$

The solutions for the amplitudes can be derived as

$$
\begin{aligned}
a_{\mathrm{H}} &= \frac{\sqrt{2\kappa_e}\left[\left(\kappa_{\mathrm{V}}-i\Delta_{\mathrm{V}}\right)\alpha+gB\beta\right]}{\left(\kappa_{\mathrm{H}}-i\Delta_{\mathrm{H}}\right)\left(\kappa_{\mathrm{V}}-i\Delta_{\mathrm{V}}\right)+\left(gB\right)^2}, \\
a_{\mathrm{V}} &= \frac{\sqrt{2\kappa_e}\left[-gB\alpha+\left(\kappa_{\mathrm{H}}-i\Delta_{\mathrm{H}}\right)\beta\right]}{\left(\kappa_{\mathrm{H}}-i\Delta_{\mathrm{H}}\right)\left(\kappa_{\mathrm{V}}-i\Delta_{\mathrm{V}}\right)+\left(gB\right)^2},
\end{aligned}
\tag{S5}
$$

with $\Delta_{\mathrm{H}}=\nu-\nu_{\mathrm{H}}$ and $\Delta_{\mathrm{V}}=\nu-\nu_{\mathrm{V}}$. Hereafter, we consider the degenerate case of the initial cavity modes, that is $\nu_{\mathrm{H}}=\nu_{\mathrm{V}}=\nu_0$, and resulting in $\Delta_{\mathrm{H}}=\Delta_{\mathrm{V}}=\Delta_\nu$ and $\Delta\nu_0=0$.

The properties of transmission can be obtained by the input-output relation, that is $a_{\mathrm{H/V,out}}=\sqrt{2\kappa_e}a_{\mathrm{H/V}}$. The total transmission spectrum of our measurement is given by

$$
T\left(\nu\right)=\frac{\left|a_{\mathrm{H}}\left(\nu\right)\hat{e}_{\mathrm{H}}+a_{\mathrm{V}}\left(\nu\right)\hat{e}_{\mathrm{V}}\right|^2}{\left|\alpha\right|^2+\left|\beta\right|^2},
\tag{S6}
$$

where $\left\{\hat{e}_{\mathrm{H}},\hat{e}_{\mathrm{V}}\right\}$ represents a pair of orthogonal polarization basis vectors, satisfying the orthogonality condition $\hat{e}_i\cdot\hat{e}_j=\delta_{ij}\left(i,j=\mathrm{H},\mathrm{V}\right)$. Note that the response lineshape is not uniform or unique; rather, it varies based on the configuration of the input/output channels [3]. Here, we focus on two specific cases: one excites a single cavity mode (either the HP mode or the VP mode), while the other simultaneously drives two cavity modes with equal strength.

S3.2 Spectral lineshape in single-mode excitation

We first study the case of single excitation. Without loss of generality, we assume that $\beta=0$, meaning that only the HP mode is driven. Substituting Eq. (S5) into Eq. (S6), we obtain

$$
T_{\beta=0}=\frac{4\kappa_e^2\left[\kappa_{\mathrm{V}}^2+g^2B^2+\Delta_\nu^2\right]}{\left(g^2B^2-\Delta_\nu^2+\kappa_{\mathrm{H}}\kappa_{\mathrm{V}}\right)^2+\Delta_\nu^2\left(\kappa_{\mathrm{H}}+\kappa_{\mathrm{V}}\right)^2},
\tag{S7}
$$

where the driving field detuning is $\Delta_\nu=\nu-\nu_0$. We examine the lineshape of the total transmission spectrum in the exceptional point (EP) and posit that $gB=\left|\Delta\kappa\right|$. According to Eq. (S7), the total transmission spectrum can be formulated as

$$
T_{\mathrm{EP},\beta=0}=\frac{4\kappa_e^2\left(\Delta_\nu^2+\kappa_{\mathrm{V}}^2+\Delta\kappa^2\right)}{\left(\Delta_\nu^2+\kappa^2\right)^2}.
\tag{S8}
$$

Hence, in the case of single-mode excitation, when $\Delta_\nu\ll\kappa_{\mathrm{V}}$, the response lineshape of the total transmission spectrum features a squared Lorentzian shape [4].

S3.3 Spectral lineshape in two-mode excitation and retrieval of eigenvalues

In our experiment, the driving field is linearly polarized light at 45° relative to the horizontal direction. In this configuration, both the HP and VP modes are simultaneously driven with equal intensity, implying that $\alpha = \beta$. Therefore, substituting Eq. (S5) into Eq. (S6), we get

$$T = \frac{2\kappa_e^2\left[\left(\kappa_{\mathrm{H}} - gB\right)^2 + \left(\kappa_{\mathrm{V}} + gB\right)^2 + 2\Delta_\nu^2\right]}{\left(g^2B^2 - \Delta_\nu^2 + \kappa_{\mathrm{H}}\kappa_{\mathrm{V}}\right)^2 + \Delta_\nu^2\left(\kappa_{\mathrm{H}} + \kappa_{\mathrm{V}}\right)^2}. \tag{S9}$$

We define $\Delta_\pm = \nu - \mathrm{Re}\{\nu_\pm\}$ and $\kappa_\pm = -\mathrm{Im}\{\nu_\pm\}$, where $\mathrm{Re}\{\nu_\pm\}$ and $\mathrm{Im}\{\nu_\pm\}$ represent the real and imaginary parts of the eigenfrequencies. Below we consider three scenarios:

Case I: $gB < |\Delta\kappa|$

In this case, we have $\Delta_+ = \Delta_- = \Delta_\nu$ and $\kappa_\pm = \kappa \mp \sqrt{\Delta\kappa^2 - g^2B^2}$. Equation (S9) can be rewritten as

$$\begin{aligned} T &= \frac{2\kappa_e^2\left[\left(\kappa_{\mathrm{H}} - gB\right)^2 + \left(\kappa_{\mathrm{V}} + gB\right)^2 + 2\Delta_\nu^2\right]}{\left(g^2B^2 - \Delta^2 + \kappa_{\mathrm{H}}\kappa_{\mathrm{V}}\right)^2 + \Delta^2\left(\kappa_{\mathrm{H}} + \kappa_{\mathrm{V}}\right)^2} \\ &= \frac{2\kappa_e^2\left[\left(\kappa_{\mathrm{H}} - gB\right)^2 + \left(\kappa_{\mathrm{V}} + gB\right)^2 + 2\Delta_\nu^2\right]}{\left(\Delta_\nu^2 + \kappa_+^2\right)\left(\Delta_\nu^2 + \kappa_-^2\right)} \\ &= 2\kappa_e^2\left[\frac{P_1}{\Delta_\nu^2 + \kappa_+^2} + \frac{P_2}{\Delta_\nu^2 + \kappa_-^2}\right], \end{aligned} \tag{S10}$$

with

$$P_1 = 1 - \frac{gB}{\kappa}\sqrt{\frac{\Delta\kappa - gB}{\Delta\kappa + gB}}, \quad P_2 = 1 + \frac{gB}{\kappa}\sqrt{\frac{\Delta\kappa - gB}{\Delta\kappa + gB}}, \tag{S11}$$

The total transmission spectrum can be observed as the superposition of two Lorentzian lineshapes, as indicated by Eq. (S10). The center frequencies of the two Lorentzian profiles are identical, corresponding to the real part of the system's eigenfrequencies, whereas their full width at half maximum (FWHM) characterizes its imaginary component.

Case II: $gB = |\Delta\kappa|$

This case corresponds to the EP, and its total transmission spectrum can be written

as

$$T_{\mathrm{EP}} = 2\kappa_e^2 \left[\frac{1}{\Delta_+^2 + \kappa_+^2} + \frac{1}{\Delta_-^2 + \kappa_-^2} \right]. \tag{S12}$$

Therefore, the total spectrum in the EP case can also be expressed as a combination of two Lorentzian lineshapes. Additionally, since $\Delta_+ = \Delta_- = \Delta_\nu$ and $\kappa_+ = \kappa_- = \kappa$, Eq. (S12) can be further simplified to

$$T_{\mathrm{EP}} = \frac{4\kappa_e^2}{\Delta_\nu^2 + \kappa^2}. \tag{S13}$$

Obviously, in the case of two-mode excitation, the total transmission spectrum in the EP follows a Lorentzian distribution, which contrasts with the situation when only a single mode is driven.

Case III: $gB > |\Delta\kappa|$

When $gB > |\Delta\kappa|$, we obtain $\Delta_\pm = \Delta_\nu \mp \sqrt{g^2B^2 - \Delta\kappa^2}$ and $\kappa_+ = \kappa_- = \kappa$. Equation (S9) can also be rewritten as

$$\begin{aligned} T &= \frac{2\kappa_e^2 \left[\left(\kappa_{\mathrm{H}} - gB\right)^2 + \left(\kappa_{\mathrm{V}} + gB\right)^2 + 2\Delta_\nu^2 \right]}{\left(g^2B^2 - \Delta^2 + \kappa_{\mathrm{H}}\kappa_{\mathrm{V}}\right)^2 + \Delta^2\left(\kappa_{\mathrm{H}} + \kappa_{\mathrm{V}}\right)^2} \\ &= \frac{2\kappa_e^2 \left[\left(\kappa_{\mathrm{H}} - gB\right)^2 + \left(\kappa_{\mathrm{V}} + gB\right)^2 + 2\Delta_\nu^2 \right]}{\left(\Delta_+^2 + \kappa^2\right)\left(\Delta_-^2 + \kappa^2\right)} \\ &= 2\kappa_e^2 \left[\frac{P_1}{\Delta_+^2 + \kappa^2} + \frac{P_2}{\Delta_-^2 + \kappa^2} \right], \end{aligned} \tag{S14}$$

while

$$\begin{aligned} P_1 &= \frac{1-b}{2\sqrt{g^2B^2 - \Delta\kappa^2}}\Delta_\nu + b, \\ P_2 &= -\frac{1-b}{2\sqrt{g^2B^2 - \Delta\kappa^2}}\Delta_\nu + b, \end{aligned} \tag{S15}$$

with $b = \left[\left(\kappa_{\mathrm{V}} + gB\right)^2 + \left(\kappa_{\mathrm{H}} - gB\right)^2 \right] \Big/ 2\left(g^2B^2 + \kappa_{\mathrm{H}}\kappa_{\mathrm{V}}\right)$. In particular, we investigate the situation near EP, setting $gB = |\Delta\kappa| + \zeta$, where ζ is a small quantity relative to κ. Then we have

$$T \approx \left(1-\frac{2\zeta\Delta\kappa}{\kappa^2}\right)\left(\frac{2\kappa_e^2}{\Delta_+^2+\kappa^2}+\frac{2\kappa_e^2}{\Delta_-^2+\kappa^2}\right)-\frac{\kappa_e^2\sqrt{2\zeta\Delta\kappa}}{\kappa^2}\frac{\Delta_+^2-\Delta_-^2}{\left(\Delta_+^2+\kappa^2\right)\left(\Delta_-^2+\kappa^2\right)}\Delta_v. \quad \text{(S16)}$$

The second term of Eq. (S16) is much smaller than the first term because $\zeta \ll \kappa$, $\Delta_+^2-\Delta_-^2 \ll \left(\Delta_+^2+\kappa^2\right)\left(\Delta_-^2+\kappa^2\right)$. Thus, in the vicinity of EP, the total transmission spectrum can be described as a combination of two concise Lorentzian profiles, expressed as

$$T \approx \left(1-\frac{2\zeta\Delta\kappa}{\kappa^2}\right)\left(\frac{2\kappa_e^2}{\Delta_+^2+\kappa^2}+\frac{2\kappa_e^2}{\Delta_-^2+\kappa^2}\right). \quad \text{(S17)}$$

It is worth noting that, unlike Eq. (S10), in this particular case, the linewidths of both Lorentzian lineshapes are identical, while the center frequencies are no longer degenerate.

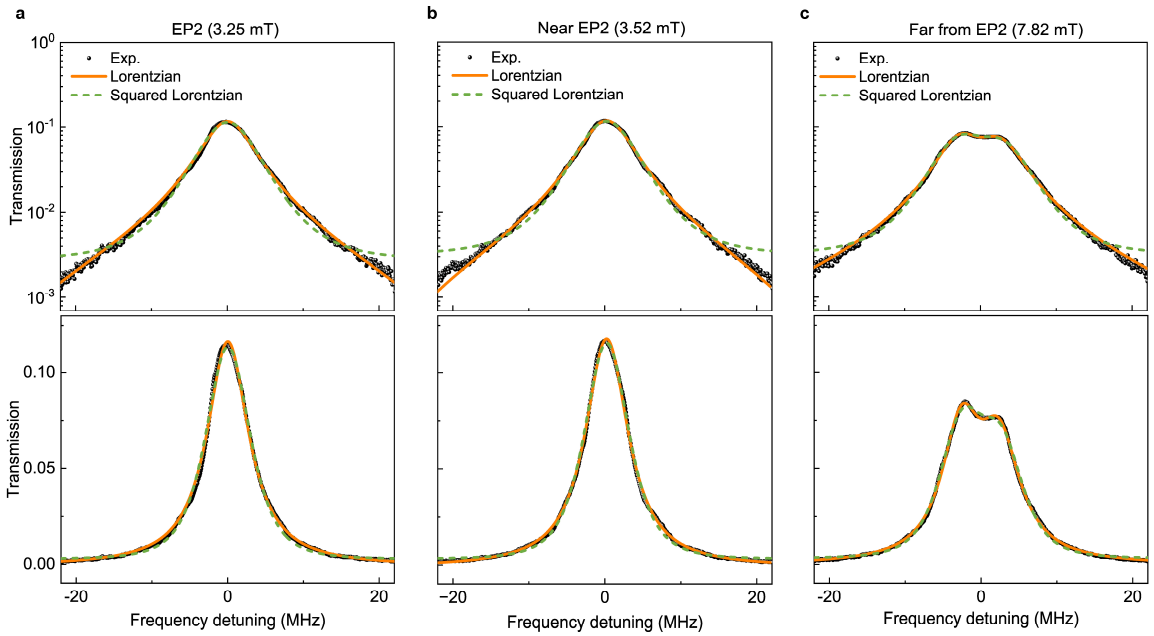

Fig. S3. Log-scale (upper row) and linear (lower row) total transmission spectra of the EP2 sensor at EP (a), near EP (b) and far away from EP (c). Dots are experimental data. The orange solid curves are fitted with two Lorentzian functions, while the dashed green curves for fitting with two squared Lorentzian lineshapes. By fitting the spectra, we obtain the frequency splitting $\Delta_+-\Delta_-=0.25$ MHz for (a), $\Delta_+-\Delta_-=1.05$ MHz for (b), $\Delta_+-\Delta_-=5.08$ MHz for (c). Here, we shift the spectra roughly to the average of two eigenfrequencies.

In summary, we prove that the total transmission spectrum of Eq. (S9) can be decomposed into a superposition of two Lorentzian lineshapes. Therefore, by fitting the total transmission spectrum using two Lorentzian profiles, we can retrieve the eigenfrequencies and the decay rates of the non-Hermitian system.

Figure S3 shows the fitting of the total transmission spectra with different theoretical lineshapes for scenarios at EP2, near EP2, and far away from EP2, respectively. We have adopted both linear and logarithmic scales to better observe the details of the fit. In accordance with our experimental parameters, $\Delta\kappa$ is much smaller than κ. Therefore, even for a large value of $\zeta = 2\Delta\kappa$, the fitting results obtained using two Lorentzian profiles remain in good agreement with the experiment data, see Fig. S3c. Furthermore, it can be observed that, in all cases, the fitting using two Lorentzian lineshapes aligns better with the experimental data than using two squared Lorentzian profiles. This proves the validity of our fitting method.

S4. Fabrication of the LC cell and the linear dichroism

The LC cell is fabricated using the LC and two glass substrates coated with Indium Tin-Oxide (ITO). The substrates are spin-coated with a photoalignment material. The ITO and anti-reflective coated glass substrates (1.5×2 cm^2) are ultrasonically bathed and UV-ozone cleaned. To form the photoalignment layer, the alignment agent SD1 (Dai-Nippon Ink and Chemicals, Japan) is dissolved in dimethylformamide (DMF) at a concentration of 0.3 wt %, and spin-coated onto the substrate. The chemical structure of SD1 is shown in Fig. S2a. After curing at 100 ℃ for 10 minutes, two pieces of substrates are separated using 6 μm spacers and sealed with epoxy glue to form a cell.

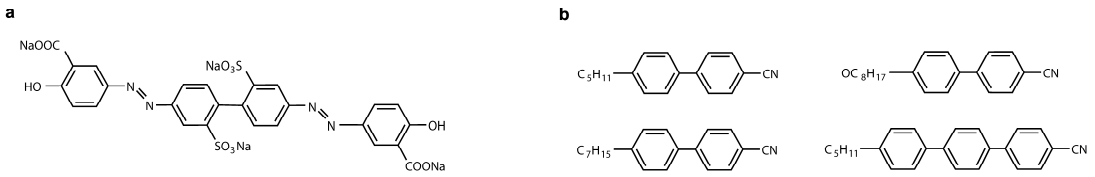

Fig. S4. Chemical structure of alignment agent and LC materials. a, Chemical structure of SD1. b, Chemical structure of nematic LC E7. The material E7 is composed of 51% 5CB (upper left), 25% 7CB (lower left), 16% 8OCB (upper right) and 8% 5CT (lower right).

The cell is then infiltrated with a nematic LC mixture E7 (HCCH, China), whose components and chemical structure are shown in Fig. S2b. The SD1-coated substrates

are exposed under ultraviolet light to create a uniform planar alignment. In the experiment shown in Fig. 2b, the orientation of SD1 is along the vertical direction.

In contrast to the conventional Hermitian MO effect using a standard Faraday FP cavity with $\Delta\kappa = 0$, the FP cavity in the loss-enhanced MO effect incorporates a home-made LC cell. Due to the anisotropy of E7, the LC cell exhibits linear dichroism, meaning differential loss between the HP and VP eigenmodes. Generally, when the light polarization is parallel to the direction of LC molecules, the absorption is slightly higher compared to the orthogonal direction. When an electric voltage is applied, the LC molecules tends to align along the direction of the electric field, but are always orthogonal to the horizontal direction. As a result, the absorption of the HP light field remains almost unchanged, while the absorption of the VP field varies with the applied voltage. In our experiments, the LC molecules are aligned along the vertical direction, meaning that the absorption of VP light is greater than that of HP direction, meaning that the absorption of VP light is slightly larger than that of HP light. This leads to $\Delta\kappa \neq 0$, as shown in Fig. 2e,f. This differential absorption is confirmed by experimental observation presented in Fig. 2d.

S5. Discussion of system parameters

S5.1 Calculation of cavity loss

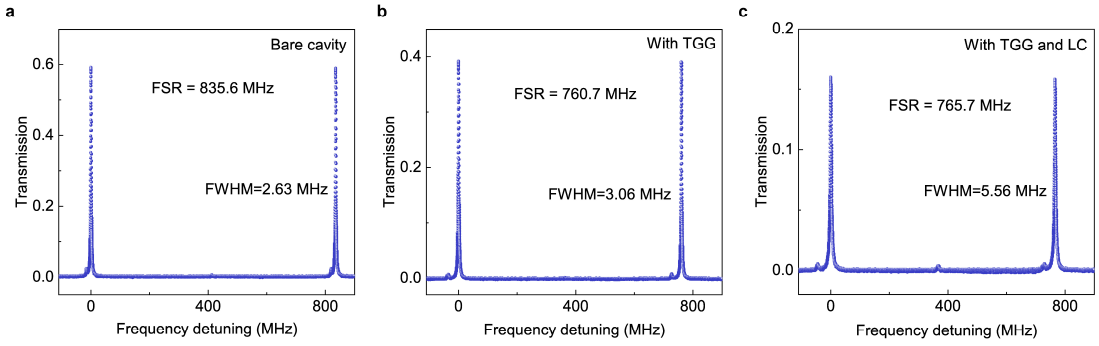

Fig. S5. Transmission spectra in three different cavities. a, Bare FP cavity. **b**, FP cavity with the TGG crystal. **c**, FP cavity with the TGG crystal and the LC cell.

The loss of the MO FP cavity can be categorized into two groups: one pertains to the external attenuation resulting from light coupling in and out through the two cavity mirrors, which we denote as $\kappa_{e,1}$ and $\kappa_{e,2}$ respectively. The other group refers to intrinsic attenuation caused by factors such as material absorption introduced by the MO crystal and the LC cell (recorded as κ_{MO} and κ_{LC}), with cavity mode mismatch

being almost ignored in our system. Thus, the total loss of the MO FP cavity is of the form of $\kappa_{\text{tot}} = \kappa_{e,1} + \kappa_{e,2} + \kappa_{\text{MO}} + \kappa_{\text{LC}}$. These attenuations can be experimentally determined by measuring the transmission of the MO crystal and the LC cell, and then using the formual:

$$e^{-2\pi\kappa_{\text{tot}}/\text{FSR}} = R_1 R_2 T_{\text{MO}}^2 T_{\text{LC}}^2, \tag{S18}$$

where FSR represents the free spectral range of the MO FP cavity and $R_{1(2)}$ is the reflectivity of the input (output) mirror. We first consider the bare FP cavity consisting of two concave mirrors. Equation (S18) reduces to $e^{-2\pi\kappa_i/\text{FSR}} = R_j \ (j = 1,2)$. In our experiment, the two mirrors are identical, leading to the equivalence $\kappa_{e,1} = \kappa_{e,2} = \kappa_e$. Based on the fitting results shown in Fig. S5a, we obtain $\kappa_e = 1.315$ MHz , corresponding to the reflectivities of $R_1 = R_2 = 99.02\%$ The calculated values are nearly the same as the factory values of 99%. If we use a cavity mirror with reflectivity higher than 99.9%, the external attenuation can be reduced to $\kappa_e = 0.315$ MHz, where the total loss is mainly determined by material absorption, leading to $\kappa_{\text{tot}} \approx \kappa_{\text{MO}} + \kappa_{\text{LC}}$.

In the cavity composed of the FP cavity and a MO crystal (i.e., the TGG crystal), the relation becomes $e^{-2\pi(\kappa_1+\kappa_2+\kappa_{\text{MO}})/\text{FSR}} = R_1 R_2 T_{\text{MO}}^2$. Based on the fitting results shown in Fig. S5b, we obtain $\kappa_{\text{MO}} = 0.43$ MHz. We can determine $T_{\text{MO}} = 99.73\%$, which is very close to the number provided by the manufactory. We measured the single pass transmittance of the LC cell (top panel of Fig. 2d in the main text). The LC-caused cavity loss (bottom panel of Fig. 2d in the main text) can be derived from the relation $e^{-2\pi\kappa_{\text{LC}}/\text{FSR}} = T_{\text{LC}}^2$. It is worth noting that LC produces different losses for HP and VP modes, resulting in a loss difference $\Delta\kappa$. This loss difference can also be adjusted by controlling the voltage applied to the LC, which plays a key role in achieving the electrically tunable loss-enhanced MO effect. Without loss of generality, we consider the HP mode, when the voltage $U = 1.924$ V, the measured loss caused by the LC is $\kappa_{\text{LC}} = 2.5$ MHz, see Fig. S5c.

S5.2 Quality factor of the MO FP cavity

The resonant frequency of a FP cavity satisfies

$$\nu_q = \frac{qc}{2L_{\text{eff}}}. \tag{S19}$$

Here, L_{eff} is the effective cavity length, q is a positive integer, and c is the speed of light. In our MO FP cavity system, $L_{\text{eff}} = n_0 L + (n_{\text{MO}} - n_0) L_{\text{MO}} + (n_{\text{LC}} - n_0) L_{\text{LC}}$, where L, L_{MO}, and L_{LC} represent the lengths of the FP cavity, the MO crystal, and the LC cell respectively, while n_0, n_{MO}, n_{LC} correspond to their respective internal refractive indices. The quality factor, indicative of the number of times photons are reflected within the cavity, bears a relationship with the loss in the MO FP cavity:

$$Q = \frac{\nu_q}{\kappa_{\text{tot}}}. \tag{S20}$$

The resonance frequency of the cavity can be selected as required. In our experiment, the resonance frequency of the cavity is approximately 3.77×10^{14} MHz for both HP and VP modes. Therefore, the quality factor of the MO FP cavity is predominantly constrained by the total loss κ_{tot}. The smaller the loss, the higher the quality factor. Without loss of generality, we also consider the HP mode. The quality factor of the bare cavity is $Q_{\text{HP}} = 1.43 \times 10^8$, based on the aforementioned cavity losses. The quality of the cavity containing the TGG crystal is $Q_{\text{HP}} = 1.23 \times 10^8$. When both the TGG crystal and the LC cell are embedded in the cavity, the cavity has a quality factor of $Q_{\text{HP}} = 0.68 \times 10^8$.

S5.3 Impact of system parameters on sensitivity

In a general model for sensors, the measured frequency shift to a small perturbation ΔB is $\delta\nu = R\Delta B + \sigma$, where $\sigma = \sqrt{R^2\sigma_B^2 + \sigma_0^2}$. The first term is the contribution from the signal ΔB. σ_B describes the signal-related noise. It is dominantly caused by the fluctuation of the current I and proportional to I. σ_0 implies the background noise and can originate from various sources, including the phase noise of the probe laser, noise in photodetector, etc. Clearly, the signal-related noise can be amplified by a large response. If the signal-related noise contribution is dominant, i.e. $R\sigma_B \gg \sigma_0$, the sensitivity enhancement benefit from the improved response will be compensate by the amplified noise. This simple model presents an apparent picture why the gain-loss non-Hermitian sensor can't improve the sensitivity by enhancing the system dynamic response, which is interpreted in terms of the Petermann factor [5]. The response improvement can only suppress the background noise σ_0.

In practical measurement, the signal is externally introduced into the system, which allows for the avoidance of these current-related noises. Therefore, theoretically, it is justifiable to solely consider the contribution arising from the background noise σ_0. The response takes the form of $R_{\mathrm{EP}} = 2g^2 B \Big/ \sqrt{g^2 B^2 - \Delta\kappa^2}$. Thus, the sensitivity can be evaluated as

$$S_{\mathrm{EP}} = \frac{\sigma_0 \sqrt{g^2 B^2 - \Delta\kappa^2}}{2g^2 B}. \tag{S21}$$

The uncertainty in the fitting is determined by this background noise. In our experiment, it is related to the spectral linewidth as $\sigma_0 \approx \kappa_{\mathrm{tot}} / M$, where M is a number determined by fitting experimental data. In our loss-enhanced magnetic sensor, we obtained $M \sim 200$. Near EP, the response formula can be simplified as $R_{\mathrm{EP}} = g \Big/ \sqrt{2B_{\mathrm{EP}} / \Delta B}$, where ΔB is a small perturbation around B_{EP} ($B_{\mathrm{EP}} = |\Delta\kappa| / g$). Thus, the sensitivity is given by an analytical expression:

$$S_{\mathrm{EP}} = \frac{\kappa_{\mathrm{tot}}}{gM} \sqrt{\frac{\Delta B}{2B_{\mathrm{EP}}}}. \tag{S22}$$

From Eq. (S22), it can be deduced that the sensitivity primarily depends on the spectral linewidth (κ_{tot}) and the coupling coefficient g. Consequently, the smaller the total loss of the system, the larger the cavity quality factor and the higher the sensitivity. Moreover, for a high reflectivity of cavity mirrors, this sensitivity is predominantly determined by the material induced loss and the response. Enhancing the coupling coefficient g can correspondingly improve the sensitivity. If Ce-doped Yttrium iron garnet (YIG) with $C_{\mathrm{V}} \sim -10^5$ rad/T/m [6] is employed, the coupling factor g can be increased by three orders of magnitude, thereby significantly enhancing the sensitivity.

Reference

1. Duan, X.Y., Wang, B., Rong, K.X. et al. Valley-addressable monolayer lasing through spin-controlled berry phase photonic cavities. *Science* **381**, 1429-1432 (2023).
2. Zvezdin, A.K., Korov, V.A. Modern magnetooptics and magnetooptical materials. Chapters 2-3, IOP Publishing Ltd (1997).
3. Hashemi, A., Busch, K., Christodoulides, D.N. et al. Linear response theory of open systems with exceptional points. *Nat. Commun.* **13**, 3281 (2022).

4. Takata, K., Nozaki, K., Kuramochi, E. et al. Observing exceptional point degeneracy of radiation with electrically pumped photonic crystal coupled-nanocavity lasers. *Optica* **8**, 184–192 (2021).
5. Wang, H., Lai, Y.-H., Yuan, Z., et al. Petermann-factor sensitivity limit near an exceptional point in a Brillouin ring laser gyroscope. *Nat. Commun.* **11**, 1610 (2020).
6. Yan, W., Yang, Y., Liu, S., et al. Waveguide-integrated high-performance magneto-optical isolators and circulators on silicon nitride platforms. *Optica* **7**, 1555–1562 (2020)